THE ASTROPHYSICAL JOURNAL, 269:715–727, 1983 June 15

THE IMPULSIVE PHASE OF SOLAR FLARES. II. CHARACTERISTICS OF THE HARD X-RAYS

JOHN LEACH[1] AND VAHÉ PETROSIAN[1]
Institute for Plasma Research, Stanford University
Received 1982 October 1; accepted 1982 November 30

ABSTRACT

We use the results of our investigation into the electron distribution in the general nonthermal models of solar flares to calculate the characteristics of the impulsive hard X-rays. We look at the height distribution, the spectrum, the polarization and directivity of the X-rays, and investigate how these X-ray characteristics are affected by the parameters defining the model. We obtain an expression for the X-ray intensity as a function of source height which is an excellent fit under certain constraints which are discussed. We then look at some recently available data with spatial resolution and show that we are able to reproduce these data adequately with our nonthermal model and to determine the values of the parameters describing the flares.

Subject headings: polarization — radiation mechanisms — Sun: flares — Sun: X-rays

I. INTRODUCTION

One resource from which we are able to gain information as to the nature of the accelerated electrons in a flare is observations of hard X-rays. The theory describing the generation of bremsstrahlung radiation from electrons is well understood (for references see the review by Brown 1975; and Kane *et al.* 1980), but there are still many difficulties to be overcome when inverting the problem (Craig and Brown 1976). There are many free parameters involved when we attempt to infer electron characteristics from the observed X-rays. Many different electron distributions are able to mimic the same X-ray output if taken over a suitable flare volume.

Until recently most experiments were concerned with the spectrum of the X-rays. As a result, early work on flare modeling dealt with simplified assumptions about the characteristics of the electrons and the flare geometry (Hudson 1972; Brown 1972*a*, *b*, 1973; Petrosian 1973; Kane 1974; Brown and McClymont 1975), with considerable attention devoted to the differences between the so-called thermal and nonthermal models. More recently these works have been elaborated upon by including the effects of a reverse current (Knight and Sturrock 1977; Emslie 1980), the photospheric albedo (Santangelo, Horstman, and Horstman-Moretti 1973; Langer and Petrosian 1977; Bai and Ramaty 1978), and a more thorough analysis of thermal models (Crannell *et al.* 1978; Brown, Melrose, and Spicer 1979; Smith and Lilliequist 1979; Smith and Brown 1980; Brown and Hayward 1981; Emslie 1981).

In order to understand more precisely the role of the electrons in flares, we need to look at the X-rays in more detail. We seek information on the polarization and directivity of the X-rays and the height distribution of the X-rays throughout the flare loop.

The instruments available on *SMM* have made available data of not only high spectral resolution but also high spatial resolution (van Beek *et al.* 1980, 1981; Hoyng *et al.* 1981*a*, *b*). Recent stereoscopic observations of limb flares have provided further data on spatial structure and directivity (Kane *et al.* 1979; Kane 1980; Kane *et al.* 1982). These, along with high spatial resolution microwave observations, are giving us previously unavailable opportunities to understand flares.

Further insight into the flare problem might be gained from observations of X-ray polarizations. Earlier modeling showed that it should be easy to distinguish between flares with nearly isotropic electron distributions and having expected polarizations of a few percent and flares with beamed electrons having polarizations of up to 80% (Brown 1972*b*; Haug 1972; Henoux 1975; Langer and Petrosian 1977; Bai and Ramaty 1978). Unfortunately, there is no facility for making polarization measurements on board the *SMM*, and past experiments have been inconclusive (Tindo, Shuryghin, and Steffen 1976 and references therein).

Our objective is to understand better the nature of the electron distribution in flares by calculating the X-rays to be expected according to a general nonthermal model and comparing these results with the available data. To obtain a reliable X-ray distribution, the transport of the electrons through the flare plasma must be treated accurately.

In a previous work (Leach and Petrosian 1981, hereafter Paper I), we have described the evaluation of the electron transport for general nonthermal models. (We did not include reverse currents; therefore, our

[1]Also Department of Applied Physics.

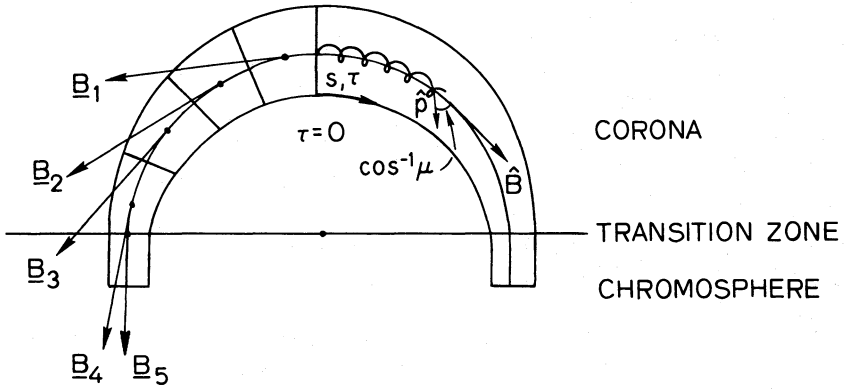

FIG. 1.—The magnetic field structure which we use for the models. The loop is semicircular in the corona and vertical throughout the thin transition zone and the chromosphere. The loop is divided into several segments with a mean magnetic field direction $\boldsymbol{B}_i$. Also shown is an electron of momentum $\boldsymbol{p}$ injected into the loop at $\tau = 0$ and spiraling along the magnetic field. μ is the cosine of the pitch angle, the angle between the direction $\hat{\boldsymbol{B}}$ of the magnetic field and $\hat{\boldsymbol{p}}$ of the electron momentum.

results are best suited to low beam current densities or to high plasma density and temperature.) Here we use these results to obtain the characteristics of the X-rays. In § II we discuss briefly the flare parameters and their relation to the expected bremsstrahlung radiation. In § III we present some general results, and in § IV we compare these results with observations to set limits on some flare parameters. In § V we summarize our conclusions.

II. GENERAL DESCRIPTION

X-rays of energy less than 1 MeV, generated during the impulsive phase of a solar flare, are the result of bremsstrahlung from electrons within that same energy range. In nonthermal models these electrons form a suprathermal beam moving through the background flare plasma. Most of the energy of the beam electrons goes into heating the ambient plasma, with only a small fraction being radiated as X-rays. One consequence of this is that the evaluation of the X-ray characteristics can be performed separately from the analysis of the beam dynamics. In Paper I we described the model with which we followed the evolution of the electron beam through the plasma. We summarize it here (cf. Fig. 1).

For simplicity we use a semicircular flare loop above the transition region with a vertical extension below it. The magnetic field strength throughout the loop, B, is given as a function of a dimensionless column depth τ from the top of the loop. Electrons with a specified energy and pitch angle spectrum are injected at $\tau = 0$ and spiral along the magnetic field lines, undergoing Coulomb collisions with the ambient plasma and adiabatic scattering by the magnetic field variations. We use the Fokker-Planck formalism to evaluate the steady state electron distribution $f(E, \mu, \tau)$ with the injected spectrum $f_0(E, \mu)$ at $\tau = 0$. Here E and $\mu = \cos\alpha$ are respectively the kinetic energy and pitch angle cosine of the electrons. With a knowledge of the electron distribution along the loop we can now proceed with the computation of the X-rays.

To compute the X-rays produced by the beam at any instant, consider an electron of energy E (momentum $\boldsymbol{p}$) at an instantaneous depth τ. The electron is scattered and emits an X-ray of energy k at an angle η to the direction $\boldsymbol{p}$. The photon is linearly polarized (Gluckstern, Hull, and Breit 1953) with its polarization vector either in the plane of emission [the $(\boldsymbol{p}, \boldsymbol{k})$-plane] or perpendicular to it. The cross sections for the production of photons are $d\sigma_{\parallel}(p, k, \eta)$ and $d\sigma_{\perp}(p, k, \eta)$, respectively, and are given by Gluckstern and Hull (1953). To these cross sections we append the Elwert (1939) Coulomb correction.

We are interested in the photon characteristics not in the plane of emission but in the overall frame of the whole flare. We define the global frame for the observations of X-rays to be the frame with the flare loop in the (y, z)-plane and the photosphere (assumed to be flat) in the (x, y)-plane (cf. Fig. 2).

We are concerned with photons of energy k emitted in a direction with polar angle Θ and azimuthal angle Φ. We also characterize these photons using the four Stokes parameters I, Q, U, and V (Chandrasekhar 1960).

We need to be able to transform the Stokes parameters from the instantaneous plane of emission [the $(\boldsymbol{p}, \boldsymbol{k})$-plane for the emitting electron] into the plane of observation [the $(\boldsymbol{k}, z)$-plane]. As the bremsstrahlung radiation is linearly polarized, we need only concern ourselves with the first three Stokes parameters, the fourth, V, being identically zero.

As an electron spirals along the magnetic field lines, the plane of emission is continually changing. At any instant the angle ψ between the plane of emission and

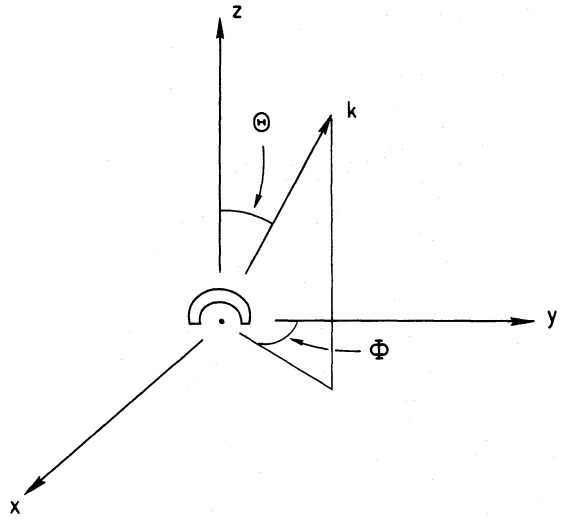

FIG. 2.—The global observational frame with the z direction being vertically outward from the surface of the Sun and the flare loop in the (y,z)-plane. A photon k is shown emitted in the Θ, Φ direction.

the plane of observation is given by

$$\cos\psi = \left(\frac{\boldsymbol{p}\wedge\boldsymbol{k}}{|\boldsymbol{p}\wedge\boldsymbol{k}|}\right)\cdot\left(\frac{\boldsymbol{k}\wedge\boldsymbol{z}}{|\boldsymbol{k}\wedge\boldsymbol{z}|}\right). \tag{1}$$

Following Chandrasekhar we define the Stokes parameters for the instantaneous beam of X-rays emitted relative to the plane of emission. For this beam the first two of these parameters are

$$i(p,k,\eta) \propto d\sigma_{\perp}(p,k,\eta) + d\sigma_{\parallel}(p,k,\eta),$$
$$q(p,k,\eta) \propto d\sigma_{\perp}(p,k,\eta) - d\sigma_{\parallel}(p,k,\eta). \tag{2}$$

If we denote by $d\sigma_1(p,k,\eta)$ and $d\sigma_2(p,k,\eta)$ the cross sections for photons emitted with polarization vectors rotated 45° from the perpendicular and parallel directions, then the third Stokes parameter is

$$u(p,k,\eta) \propto d\sigma_1(p,k,\eta) - d\sigma_2(p,k,\eta). \tag{3}$$

As shown by Haug (1972), the values of the three Stokes parameters in the plane of observation (the primed quantities) are obtained by the transformation relations

$$i'(p,k,\eta) = i(p,k,\eta),$$
$$q'(p,k,\eta) = q(p,k,\eta)\cos 2\psi,$$
$$u'(p,k,\eta) = u(p,k,\eta)\sin 2\psi. \tag{4}$$

The Stokes parameters for the radiation of energy k in the direction (Θ,Φ) from a depth τ is obtained by integrating over all the contributing electrons. We thus obtain

$$\begin{bmatrix} I \\ Q \\ U \end{bmatrix}_{\tau}(k,\Theta,\Phi)$$
$$= \int_{\mu=-1}^{1} d\mu \int_{\phi=0}^{2\pi} d\phi \int_{E=k}^{\infty} dE A(\tau) f(E,\mu,\tau) v(E)$$
$$\times n(\tau)\begin{bmatrix} i' \\ q' \\ u' \end{bmatrix}(p,k,\eta). \tag{5}$$

Integration of these equations over all depths τ will give the Stokes parameters for the radiation from the whole loop. Here ϕ is the azimuthal angle of the electron about the magnetic field line, $A(\tau)$ is the cross sectional area of the loop at the depth τ, $v(E)$ is the velocity of the electron of energy E, and $n(\tau)$ is the number density of ambient plasma protons at depth τ. The relationships between the direction (Θ,Φ) and the angles η and ψ are complex functions of the electron's pitch angle $\alpha = \cos^{-1}\mu$, azimuthal angle ϕ, and the direction of the magnetic field relative to the z axis.

To analyze the height distribution of the X-rays from our models, we divide the flare loop into adjoining segments, each a small arc of the coronal loop or a part of the vertical chromospheric loop. In this case we find it more informative to use Stokes parameters given with respect to frames other than the global frame which is the one that we use when we consider the radiation from the whole flare.

For each segment the integration of equation (5) over the appropriate range of values of τ can be simplified as follows. For each segment we define a mean magnetic field direction $\boldsymbol{B}_i$ (say, in the direction of the field at the center of the segment; cf. Fig. 1). We take this to be the polar direction for the ith segment and evaluate the Stokes parameters of the individual segment in the (local) $(\boldsymbol{k},\boldsymbol{B}_i)$-plane. For a sufficiently short segment in which the curvature of the magnetic field would be negligible, we would have azimuthal symmetry of the electron distribution about the field direction $\boldsymbol{B}_i$. In this case the third Stokes parameter would be identically zero (Haug 1972). For our curved segments (cf. Fig. 1) the electron distribution will be close to being azimuthally symmetric about the polar direction, and consequently the value of the Stokes parameter U will be negligible.

For each segment, then, we can use the Stokes parameters to obtain the directivity and the degree of linear

polarization. Let

$$\bar{I}_i(k) = \left(\frac{1}{4\pi}\right) \times \int_{\Theta=0}^{\pi}\int_{\Phi=0}^{2\pi} I_i(k,\Theta,\Phi)\sin\Theta\, d\Theta\, d\Phi \quad (6)$$

be the average value of $I_i(k,\Theta,\Phi)$ in the ith loop segment. We then define the directivity $D_i(k,\Theta,\Phi) = I_i(k,\Theta,\Phi)/\bar{I}_i(k)$ and the degree of polarization

$$\pi_i(k,\Theta,\Phi) = \frac{\left[Q_i(k,\Theta,\Phi)^2 + U_i(k,\Theta,\Phi)^2\right]^{1/2}}{I_i(k,\Theta,\Phi)}. \quad (7)$$

The inclination of the major axis of the ellipse of polarization vectors to the plane of observation, the $(\boldsymbol{k}, \boldsymbol{B}_i)$-plane is given by

$$\omega_i(k,\Theta,\Phi) = \frac{1}{2}\tan^{-1}\left\{\frac{U_i(k,\Theta,\Phi)}{Q_i(k,\Theta,\Phi)}\right\}; \quad (8)$$

and as U_i is small relative to Q_i, ω_i is close to zero or to $\pi/2$ according to whether Q_i is positive or negative. Thus, the direction of linear polarization is close to being either in the $(\boldsymbol{k}, \boldsymbol{B}_i)$-plane or perpendicular to it.

III. RESULTS

In this section we present some general results on the spectrum, directivity, and polarization of the X-rays and on the variation of these with height through the loop for the general nonthermal models. As shown in Paper I, these models are classified by the spectrum and pitch angle distribution of the electrons and the parameter $d\ln B/d\tau$ along the loop. We inject electrons with a power law spectral index δ and a Gaussian distribution in pitch angles;

$$F_0(E,\mu) = AE^{-\delta}\exp\{-\alpha^2/\alpha_0^2\}. \quad (9)$$

The Fokker-Planck method gives the electron distribution throughout the loop: $F(E,\mu,\tau)$, and equation (5) gives the variation with τ of the Stokes parameters and therefore gives a complete description of the characteristics of the X-rays.

The X-ray results may then be classified according to the three parameters $d\ln B/d\tau$, δ, and α_0^2. We shall be describing the results for a selection of nine models which allow us to observe the dependence of the X-rays on each of the three parameters. The models are given in Table 1.

As is evident from equation (5), at each level τ the X-ray spectrum is that of a thin-target model for the appropriate electron distribution at that level. In particular, around $\tau = 0$ (i.e., at the top of the loop) where the electron distribution is very close to the injected spectrum (eq. [9]), we expect an X-ray spectrum with spectral index $\gamma \approx \delta + 1.0$ (cf., e.g., Brown 1971). On the other hand, the spectrum of the spatially unresolved (i.e., integrated over all τ) X-rays should be the spectrum of a thick target model (cf., e.g., Brown 1972*b*, and Paper I, eqs. [23]–[25]) with $\gamma \simeq \delta - 1/2$. The last two columns of Table 1 give $\gamma_{\rm top} - \delta$ and $\delta - \gamma_{\rm total}$ for the nine models. As can be seen, the values of $\gamma_{\rm top} - \delta$ are very near to their expected value of 1.0. Any deviation can be accounted for by the uncertainty in the determinations of $\gamma_{\rm top}$ (taking a best power law fit introduces an uncertainty of approximately 0.1) and by the finite column depth of the top segment. The values of $\delta - \gamma_{\rm total}$ deviate from their expected value of 0.5 consistently with the rate of convergence of the magnetic field. This arises from uncertainties in the determinations of $\gamma_{\rm total}$ and because the expected values are approximations valid primarily for uniform magnetic fields.

This is one test of the accuracy of the numerical program. We have also tested the numerical results further by comparing our results for a uniform and straight tube model with earlier semianalytic results (Brown 1972*b*; Haug 1972; Langer and Petrosian 1977). These works did not take into account the dispersion in pitch angles of the electrons. Therefore, they give results which can serve as order-of-magnitude indicators of the polarization and directivity. With these we find good agreement.

TABLE 1

MODELS

No.	δ	$\frac{d\ln B}{d\tau}$	α_0^2	$\gamma_{\rm top} - \delta$	$\delta - \gamma_{\rm tot}$
1.....	3	0	∞	1.0	0.6
2.....	4	0	∞	1.0	0.5
3.....	5	0	∞	1.0	0.5
4.....	5	0	0.4	1.1	0.6
5.....	5	0	0.04	0.9	0.6
6.....	5	5×10^4	0.4	0.8	0.4
7.....	5	10^5	0.4	0.7	0.15
8.....	5	10^5	0.04	0.6	0.4
9.....	5	10^5	∞	0.9	0.0

NOTE.—Table 1 shows the models referred to in the text with the values of the three input parameters δ, $d\ln B/d\tau$, and α_0^2 which determine them. Also shown are the values of $\gamma_{\rm top} - \delta$ and $\delta - \gamma_{\rm tot}$, where $\gamma_{\rm top}$ is the photon spectral index in segment 1 and $\gamma_{\rm tot}$ is the spectral index for the whole flare. The value of $d\ln B/d\tau$ quoted is valid only for the coronal magnetic field. Values of 0, 5×10^4, and 10^5 correspond to 1, 25, and 625-fold increases in the magnetic field strength from the top of the loop to the transition zone, respectively. The value of $\alpha_0^2 = \infty$ corresponds to a uniform distribution in pitch angle between $\mu = 0$ and $\mu = +1.0$.

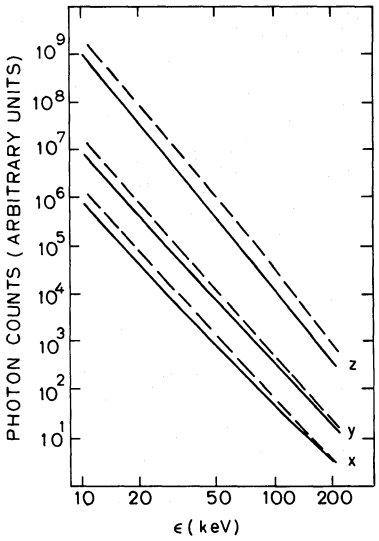

FIG. 3

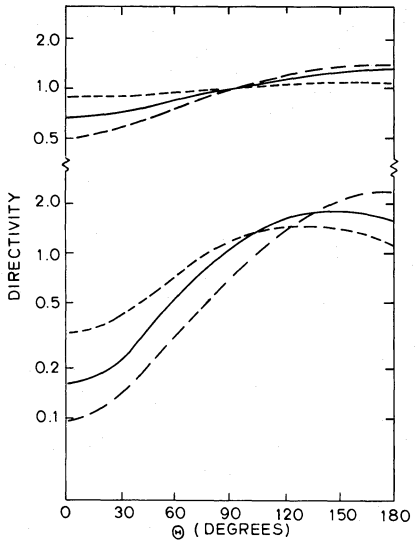

FIG. 4

FIG. 3.—X-ray spectra in the x, y, and z directions for model 3 (*solid lines*) and model 5 (*dashed lines*). The differences between the spectral indices of models 3 and 5 in each direction are small and are less than the uncertainties encountered in fitting a best-fit power law to the data. The spectral indices in the x, y, and z directions are 4.4, 4.4, and 4.85, respectively.

FIG. 4.—X-ray directivity as a function of the polar angle Θ. Zero degrees is the vertical direction away from the photosphere. Shown are the results for models 3 (*solid lines*), 5 (*dashed lines*), and 9 (*dotted lines*) at photon energies of 22 keV (*upper curves*) and 210 keV (*lower curves*).

a) *Integrated X-Rays*

Before we present the results for the variation of the spectrum, directivity, and polarization with τ, we shall describe briefly these characteristics for the X-rays integrated over the whole loop. We do this because most of the observations collected so far have not resolved the bursts spatially.

1. *Spectrum.*–As mentioned above, the total spectrum is essentially that of a thick target, as shown in Table 1.

2. *Directivity.*—Figure 3 shows the expected spectra as viewed from three directions, x, y, and z, for models 3 and 5. The effect on any of the spectra from the possible variation of the parameters α_0^2 and $d \ln B/d\tau$ would be small and no more than the uncertainty from the fitting of a best-fit power law.

Figure 4 shows the variation with Θ of the X-ray directivity at 22 keV and 210 keV for models 3, 5, and 9. In all instances the X-rays are emitted primarily into the downward-facing hemisphere. The degree of beaming is less for models with larger α_0^2 or $d \ln B/d\tau$ as the electron distribution is more nearly isotropic for these models.

3. *Polarization.*—In Figure 5 we show the variation of the photon polarization (in the y-direction) with Θ at photon energies of 16, 50, and 102 keV. As expected, model 3 with large α_0^2 and model 8 with large $d \ln B/d\tau$ have smaller degrees of polarization than model 5. In comparison, though, with Figures 2 and 3 of Langer and

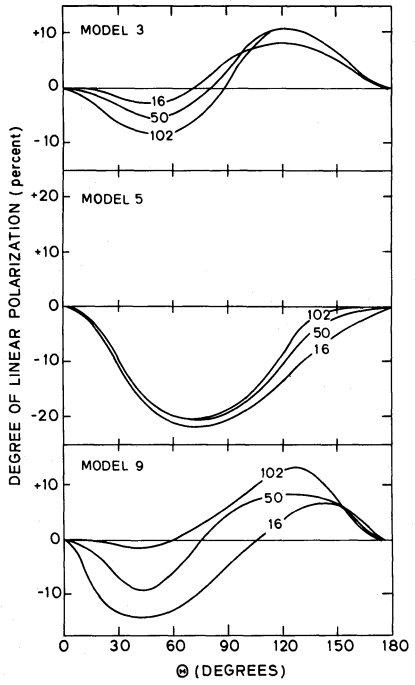

FIG. 5.—X-ray polarization as a function of the polar angle Θ. Zero degrees is the vertical direction away from the photosphere. Shown are the results for models 3, 5, and 9 at photon energies 16, 50, and 102 keV.

Petrosian (1977), our polarizations are small. This is because we have a loop rather than a straight tube and because we have included the effects of both pitch-angle diffusion and, for model 8, magnetic trapping in our analysis.

b) *Variation with Depth*

We now present the variation with τ of the X-ray parameters for the models in Table 1.

The variation with height or depth along the loop can be obtained once the variation of the ambient density along the loop is specified: $d\tau = 2\times 10^{-23}\, n(s)\, ds$ (cf. Paper I). We will be using such a relationship in the next section when we compare our results with observations.

1. *Spectrum.*—At each height the spectrum of the X-rays integrated over both angles Θ and Φ is, in general, a representative spectrum. This is especially true at low energies where the relativistic beaming effects are insignificant. In Figure 6 we show spectra at various values of τ throughout the loop for models 1, 3, 5, and 9. Also shown is the spectrum for the whole loop.

The variation of the spectrum from a thin target spectrum at the top toward a thick target spectrum for the whole loop is clearly evident in these figures.

2. *Relative intensity.*—The rate at which the beam generates photons depends upon the electron distribution and thus on the three input parameters δ, α_0^2, and $d\ln B/d\tau$. We define the X-ray intensity as $I(k,\tau)$, the fraction of the total counts emitted per unit column depth at a depth τ and at photon energy k. Figures 7–9 show the variation of $I(k,\tau)$ with τ and the effects of the input parameters.

Figure 7 gives $I(k,\tau)$ versus τ at $k=16$ and 50 keV and for models 1, 2, and 3. The intensity is approximately constant for $\tau/k^2 \ll 1$. For $\tau/k^2 \gg 1$, the intensity decreases rapidly (approximately as a power law in τ), because, as shown in Paper I, the flux of electrons responsible for photons of energy k, (that is, electrons with energy $E \gtrsim k$) decreases rapidly when $\tau/E^2 \gg 1$. For large τ/k^2 we obtain $d\ln I/d\ln\tau \simeq -\delta/2$, independent of k. That we expect this type of dependence of $\ln I$ on $\ln\tau$ can be seen with reference to the results of Paper I. Note that

$$I(k,\tau)\, d\tau = \int_{E=k}^{\infty} F(\tau,E)\, d\sigma(E,k)\, dE\, d\tau. \quad (10)$$

From equation (21) of Paper I we see that the τ dependence of $F(\tau,E)$ is of the form $[1+\tau(E+1)/E^2]^{-\delta/2-1/2}$. If we approximate the cross section by a delta function, i.e., $d\sigma(E,k)=\delta(k-E)$, then $I(k,\tau) \propto [1+\tau(k+1)/k^2]^{-\delta/2-1/2}$. If, alternately, the cross section is taken as being approximately constant, we obtain

$$I(k,\tau)\, d\tau \propto \int_{E=k}^{\infty} F(\tau,E)\, dE\, d\tau.$$

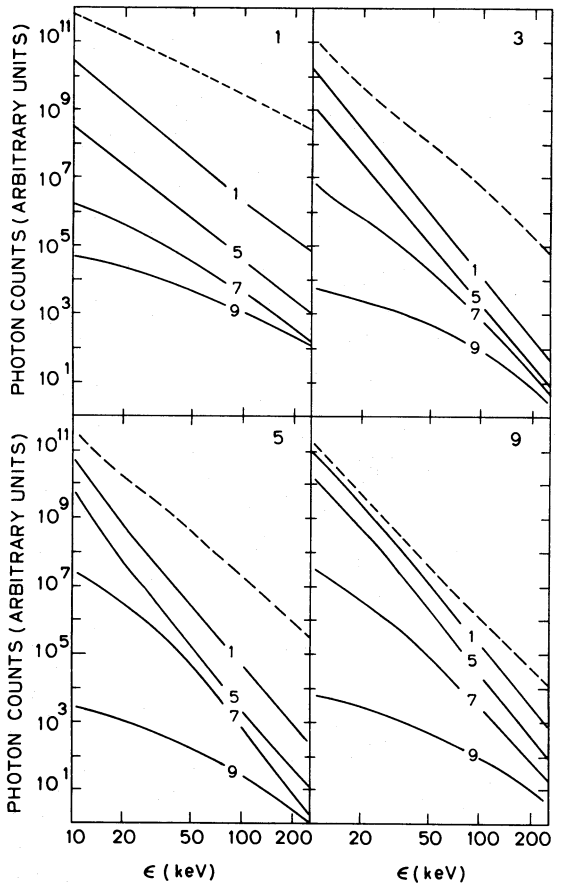

FIG. 6.—X-ray spectrum at four positions throughout the loop and for the whole loop (*dashed lines*), for models 1, 3, 5, and 9 as marked in the top right-hand corner of each box. The four solid lines in each box correspond to segments 1, 5, 7, and 9 at column depths of $3.4(+17)$ cm^{-2} [$\tau = 6.8(-6)$], $2.6(+18)$ cm^{-2} [$\tau = 5.1(-5)$], $1.3(+20)$ cm^{-2} [$\tau = 2.5(-3)$], and $4.6(+21)$ cm^{-2} [$\tau = 9.2(-2)$], respectively. The lines are separated to show the evolution of the spectrum with increasing depth, and their vertical positions do not correspond to the relative X-ray intensity at each depth.

It can then be seen that for large values of $\tau(k+1)/k^2$, these extreme assumptions about the cross section give $d\ln I/d\ln\tau = -\delta/2-1/2$ and $-\delta/2+1/2$, respectively. We obtain a constant value for $d\ln I/d\ln\tau$ at large $\tau(k+1)/k^2$ which lies within these limits.

For all photon energies in our range from 10 keV to 210 keV, we find that the results of models 1, 2, and 3 are very well approximated at large depths by the form $I(k,\tau) \propto [1+\tau(k+1)/k^2]^{-\delta/2}$. Writing $I(k,\tau) = a(\delta,k)\,[1+\tau(k+1)/k^2]^{-\delta/2}$ and recalling that $I(k,\tau)$ is, by its definition, normalized, integrating over τ from $\tau=0$ to $\tau=\infty$ gives the relationship

$$a(\delta,k) = (\delta/2-1)\big[(k+1)/k^2\big].$$

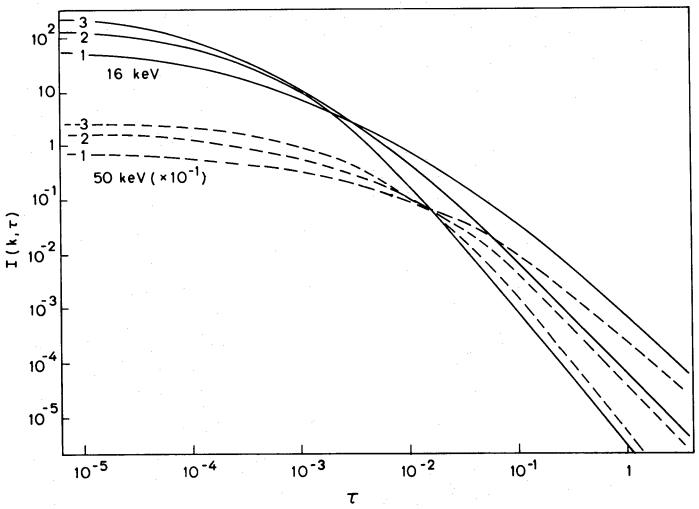

FIG. 7.—The fraction of the total number of counts emitted per unit column depth, $I(k,\tau)$, against τ, at 16 and 50 keV for models 1 ($\delta = 3$), 2 ($\delta = 4$), and 3 ($\delta = 5$). At large values of τ the slopes $d[\ln I(k,\tau)]/d\ln\tau = -\delta/2$ and are independent of energy.

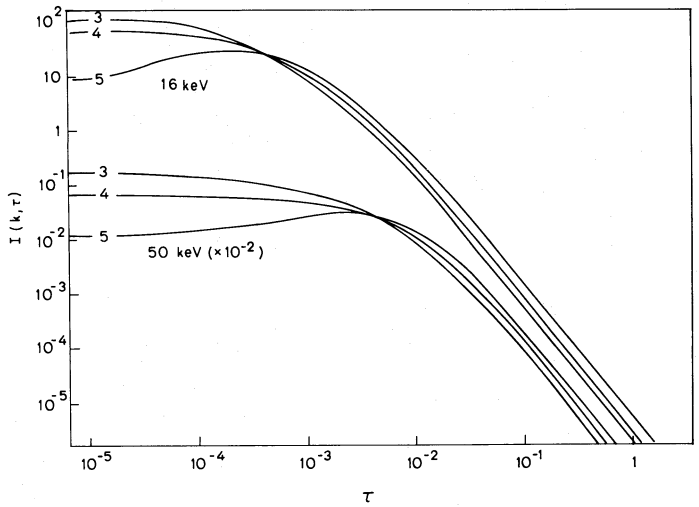

FIG. 8.—As Fig. 7, but for models 3 ($\alpha_0^2 = \infty$), 4 ($\alpha_0^2 = 0.4$), and 5 ($\alpha_0^2 = 0.04$). At large values of τ the slopes are independent of α_0^2.

We therefore obtain the form

$$I(k,\tau) = \frac{(\delta/2-1)\left[(k+1)/k^2\right]}{\left[1+\tau(k+1)/k^2\right]^{\delta/2}}. \qquad (11)$$

Though equation (11) was obtained based on the behavior of $I(k,\tau)$ at large τ, we find that it can be very accurate for small τ and all photon energies with some appropriate constraints on the parameters α_0^2 and $d\ln B/d\tau$.

In Figure 8 we show the effect of the parameter α_0^2. The amount of energy that an electron radiates as it travels unit distance measured parallel to the magnetic field depends inversely on the electron's pitch angle. Thus, as a narrow beam rapidly broadens within the plasma, the photon counts per unit τ can, initially, increase. Figure 8 clearly shows this effect. Also mentioned in Paper I was the tendency of the electron beam, below depths where $\tau/E^2 \approx 1$, to have lost any information as to its pitch-angle distribution at $\tau = 0$. Thus below a depth where $\tau/k^2 \approx 1$, the X-ray intensity profiles for different α_0^2 are essentially identical. A consequence of all this is that equation (11) can be accurately extended toward $\tau = 0$ for beams with $\alpha_0^2 \gtrsim 0.3$ and is accurate for all beams below a depth $\tau/k^2 \approx 1$ (corresponding to a column depth of 2×10^{19} cm^{-2} for 10 keV photons).

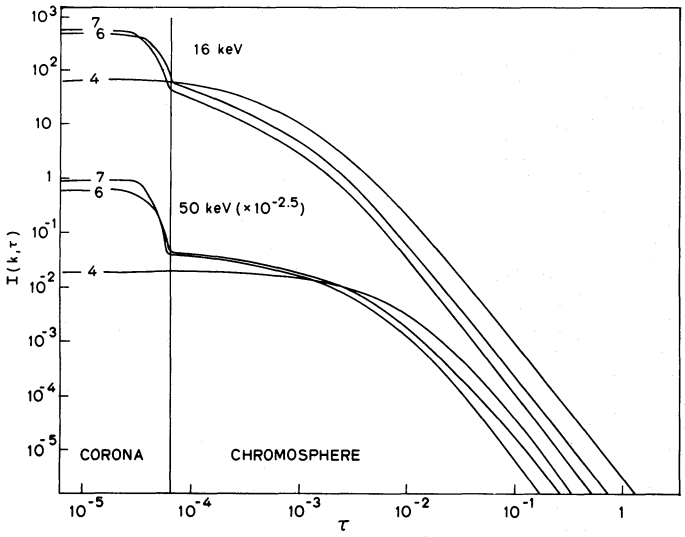

FIG. 9.—As Fig. 7, but for models 4 ($d \ln B/d\tau = 0$), 6 ($d \ln B/d\tau = 5 \times 10^4$), and 7 ($d \ln B/d\tau = 10^5$). The transition zone is marked in at $\tau = 6.3$ (-5) [$N_{TZ} = 10^{18.5}$ cm^{-2}].

In Figure 9 we show the effect of magnetic trapping on the X-rays. We specify a constant $d \ln B/d\tau$ throughout the coronal loop but do not continue it below the transition zone. Thus the magnetic trapping is all coronal trapping. Figure 9 shows that a relatively small increase in the strength of the magnetic field within the loop can cause a large increase in the X-ray intensity in the coronal loop. It requires only a moderate degree of trapping (a 25-fold increase in the magnetic field strength within the coronal part of the loop is sufficient) to increase the intensity at the top of the loop by an order of magnitude. Thus the distribution of low-energy hard X-rays throughout the loop (energies of 10–20 keV, say, such as are imaged by HXIS) is particularly sensitive to even small amounts of coronal trapping.

3. *Directivity and polarization.*—To obtain large X-ray directivities and polarizations, it is necessary to have a highly collimated electron beam. Conversely, a nearly isotropic electron distribution will give rise to X-rays of negligible directivity and polarization.

In Figures 10 and 11 we show the directivity and polarization at 16 and 102 keV at several heights for model 5, which has the most strongly collimated electron beam and a uniform magnetic field and consequently gives the largest directivities and degrees of polarization.

To facilitate the discussion of the results, we define a directivity ratio D, which is the ratio of the maximum to minimum directivities at a given height for a given photon energy. The directions of maximum and minimum directivity are usually antiparallel.

As can be seen for model 5, at the top of the coronal loop the X-rays are highly polarized and most highly directed. The directivity ratios at 16 keV and 102 keV are approximately 9 and 40, respectively, with the X-rays beamed primarily in the same direction as the electrons. The degree of linear polarization reaches a maximum of 85% for both energies in a direction normal to the direction of the electron beam.

We find that, throughout all our models, the values for the polarization and directivity are essentially independent of the azimuthal angle in the observation frame. This is one of the rewards of using the local observation frames, as described in § II.

At the bottom of the coronal loop, at a column depth of 3×10^{18} cm^{-2} ($\tau/k^2 = 0.06$ for $k = 16$ keV; $\tau/k^2 = 0.002$ for $k = 102$ keV), the X-rays are still highly directed. The directivity ratios are 7 and 40 at 16 keV and 102 keV, respectively. The degree of linear polarization is still high at 70%–82% for the two energies shown. It is not until a column depth of approximately 10^{20} cm^{-2} ($\tau/k^2 \simeq 2.0$ for 16 keV) is reached that the X-rays start to become significantly more isotropic; both the directivity and polarization fall as the source moves deeper into the chromosphere. At a depth of $\tau/k^2 \approx 2.0$, the directivity ratios have fallen to 2 and 9 for 16 and 102 keV photons, respectively; and the degrees of polarization are 9% and 20%, respectively.

In contrast to model 5, which gives the largest directivity and polarization, model 3 has an injected beam which is isotropic in the forward pitch angles, and model 8 has a strongly converging coronal magnetic field.

For model 3 (Fig. 12) the directivity ratio for 16 keV photons coming from any depth within the loop does not exceed a value of 2, and for 102 keV photons it does not exceed a value of 6. The X-rays from the top of the

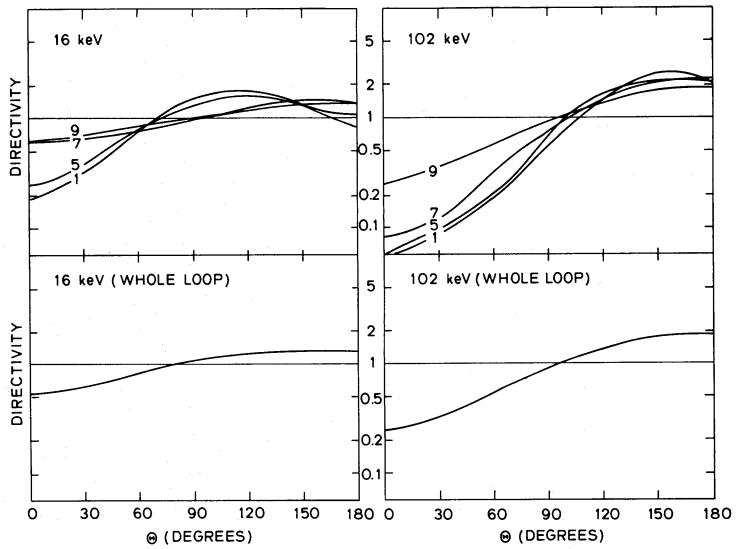

FIG. 10.—The directivity $I(k,\Theta,\Phi)/\bar{I}(k)$ as a function of Θ for $\Phi = 90°$ (the x-direction) at four heights and at two energies, 16 keV and 102 keV, for model 5. Θ is the polar angle in the local observation frame, and 0° is always into the upward-looking hemisphere, that is, away from the photosphere. The curves are labeled according to the segment of the loop to which they refer. Segment 1 is at the top of the coronal loop and has an average column depth of $3.4(+17)$ cm^{-2} [$\tau = 6.8(-5)$], segment 5 is the transition zone at a column depth of $3.2\ (+18)$ cm^{-2} [$\tau = 6.4(-4)$], segments 7 and 9 are in the chromosphere at column depths of $1.3(+20)$ cm^{-2} [$\tau \simeq 2.5(-3)$] and $4.6(+21)$ cm^{-2} [$\tau = 9.2(-2)$], respectively. Also shown is the directivity for the whole loop at these two energies.

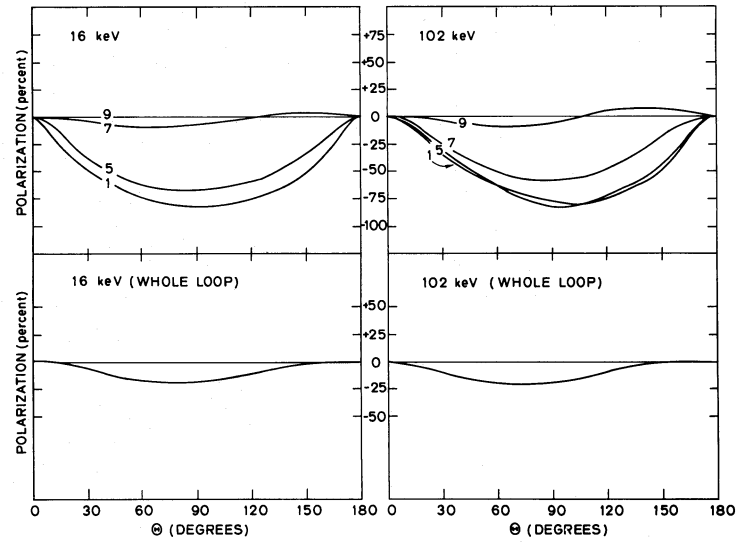

FIG. 11.—Same as Fig. 10, but for the degree of linear polarization

coronal loop are about 30% polarized at all energies from 16 keV through 102 keV. The polarization falls only slowly throughout the coronal loop, but then falls rapidly in the denser chromosphere. The polarization has fallen to 6% for 16 keV photons by the time the source has reached a column depth of 10^{20} cm^{-2}, and to 10% for 102 keV photons for a source at or below a depth of 10^{21} cm^{-2}. Looking at the loop as a whole, the polarization is about 10%–15% for a broad range of photon energies.

In model 8 (Fig. 13) the strongly converging coronal magnetic field rapidly broadens and reflects the electron beam. In the corona the photons are nearly isotropic, being only slightly directed either parallel or antiparallel to the initial electron beam. The degree of polarization increases slightly with depth within the corona. This

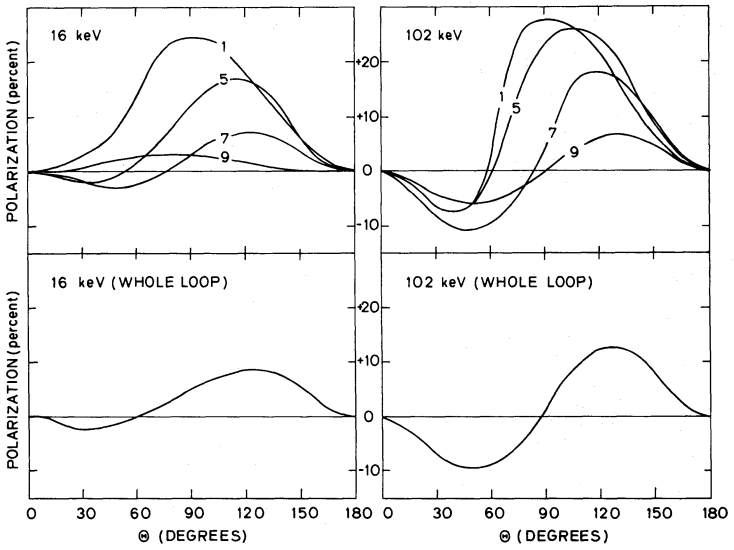

FIG. 12.—As Fig. 11, but for model 3. Note the different scale from Fig. 11

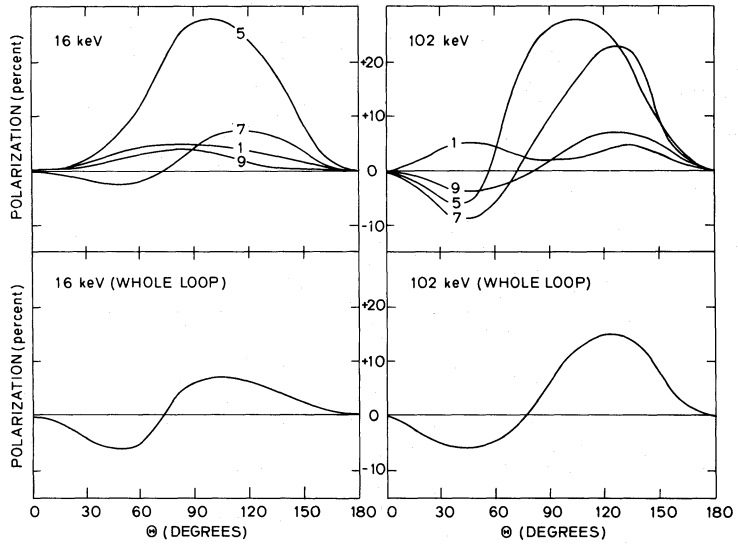

FIG. 13.—As Fig. 12, but for model 8

then falls as the source moves into the chromosphere. The average degrees of polarization for the whole loop are 7% at 16 keV and 15% at 102 keV.

IV. OBSERVATIONS

In this section we compare the results described in the previous section with observations which have spatially resolved the X-ray bursts. Our aim is to use the observations to put limits on the model parameters and thus to come up with models which fit the observations. First we need to convert our results from variations with column depth τ into variations with height. We do this by specifying the variation of the density throughout the loop. We assume a constant density from the top of the loop to the top of the transition region, which is at a column depth of N_{TZ}. Below the loop we have a thin transition region with rapidly increasing density and below that a chromosphere with a density scale height $H_n = 2000$ km. We specify a constant $d \ln B/ds$ throughout the whole loop, where s is the distance measured in cm from the top. Since the coronal density is much less than the chromospheric density and the length of the curved coronal loop is much larger than the length of the vertical chromospheric section, the immediate effects of any magnetic field convergence are

unimportant except in the corona. The values of $d \ln B/d\tau$ quoted refer to the coronal portion of the loop.

We now look at some recent observations by the hard X-ray imaging spectrometer (HXIS) experiment on board the *SMM* (Hoyng *et al.* 1981*a*) and the stereoscopic observations of Kane *et al.* (1979, 1982).

A) The HXIS experiment has the best available spatial resolution but is limited to imaging X-rays of 30 keV or less. Because of the significant contamination from thermal soft X-rays at and below 10 keV, the interpretation of the HXIS results becomes more complicated. Furthermore, the effect of the photospheric albedo may be significant for these observations. In a subsequent paper (in collaboration with Steve Langer), we shall consider the albedo effect and comment on the HXIS results in more detail. Here we just point out that the fact that many of the X-rays even at low energies come from what are expected to be the footpoints of the loop indicates that low-energy electrons must be able to penetrate to those depths. In terms of our model, we can use the figures given in Table 1 of Hoyng *et al.* (1981*a*) to put an upper limit on the transition-zone column depth. The ratios of counts in region B to regions A and C require $N_{TZ} \lesssim 2 \times 10^{19}$ cm^{-2} for their flare of 1980 April 10.

B) Information on the spatial distribution of the X-rays can also be obtained by stereoscopic observations of partially occulted limb flares such as those obtained by Kane and his collaborators using the *International Sun-Earth Explorer 3* (*ISEE 3*) and the *Pioneer Venus Orbiter* (*PVO*). These observations do not have the resolution of the HXIS experiment but contain more spectral information and, being of limb flares, are not affected by the albedo effects. We now discuss two such flares.

1. *Flare of 1978 October 5* (Kane *et al.* 1979). This flare was estimated to be 15° behind the limb for *ISEE 3*, which could therefore see those parts of the flare at altitudes of $h \geq 25{,}000$ km above the photosphere. The PVO was able to see this flare down to an altitude of $h \approx 700$ km. This flare was also analyzed by Brown, Hayward, and Spicer (1981) (hereafter BHS). We use a similar model to analyze this flare, but with the use of our full-beam dynamics and fully relativistic photon cross sections we are able to improve upon the model used by BHS.

In conjunction with the above height information, *ISEE 3* observed a power-law photon spectrum with an index $\gamma_{ISEE} \approx 5.0$ over the 5–50 keV range; while in the 50–500 keV range, the *PVO* observed $\gamma_{PVO} \approx 3$. The total *PVO* flux above 50 keV is approximately 600 times the corresponding *ISEE* flux obtained by extrapolating the *ISEE 3* spectrum to 500 keV. Alternately, extrapolating the *PVO* spectrum down to 5 keV would give a *PVO* to *ISEE 3* flux ratio of 6 over the 5–50 keV range.

As shown in Table 1, the difference between the spectral index from the top of a loop and that for the whole loop is expected to be about 1.5. We find that if we use a narrow injected beam ($\alpha_0^2 = 0.03$) with $\delta = 3.9$ and have no magnetic trapping, we are able to obtain a best fit of $\gamma_{top} = 4.9 \approx \gamma_{ISEE\ 3}$ and $\gamma_{tot} = 3.2 \approx \gamma_{PVO}$. Considering the observational uncertainties, this is a satisfactory fit. Using the *PVO/ISEE 3* flux ratio of 600, we now find that the column depth from the top of the loop down to the altitude $h = 25{,}000$ km must be close to 8×10^{18} cm^{-2}.

The column depth derived here is roughly a factor of 3 larger than that obtained by BHS. If we assume, with BHS, a length of 20,000 to 30,000 km for the segment of the loop above 25,000 km, we obtain a coronal density of 3×10^9 cm^{-3}. This higher density may alleviate some of the difficulties discussed by BHS regarding the flux-limiting role of the reverse current.

Having obtained our model, let us now look at the expected polarization. From the top (thin target) 8×10^{18} cm^{-2} of the loop, we expect very high degrees of polarization, i.e., 70% at 10 keV, increasing to 83% at 50 keV and falling to 60% at 210 keV. Had the *ISEE 3* spacecraft been equipped with a polarization-measuring device, it could easily have detected such high polarizations. For the bulk of the loop as seen by *PVO*, the degrees of polarization at the same energies would have been 6%, 10%, and 10%, respectively. Obviously, then, stereoscopic polarization measurements could provide decisive further constraints on the models.

Had this flare been seen by the HXIS experiment, it would have appeared brighter by a factor of approximately 20 at the footpoints than at the top of the loop in the energy range 11.5–30 keV. This result is not incompatible with, for example, the observations of Hoyng *et al.* (1981*a*).

2. *Flares of 1979 November 5* (Kane *et al.* 1982). In this series of observations, *PVO* saw three flares, one precisely on the limb, one 4°.3 behind the limb, and the third 4°.8 behind the limb. All three flares were in full view of *ISEE 3*. Though not all of the same size when seen by *ISEE 3*, the three flares did appear to be congruent; that is, the spectral shape of each flare was essentially the same whether seen by *ISEE 3* or *PVO*, and the spectral shapes of one flare to the next were similar. Because of this congruency, we may treat the three observations as if they were separate observations of one "typical" flare. We then have, with reference to Figure 3 of Kane *et al.* (1982), a rough estimate of the height distribution of 100–200 keV X-rays within our "typical" flare. The mean spectral index over this energy range is 3.15.

The third flare was sufficiently occulted that *PVO* could see only those parts of the flare which were at altitudes greater than 2500 km above the photosphere. The rapidly changing X-ray source brightness with height

requires that the transition zone be located very close to this height.

The constraints which we need to satisfy then in constructing our model are:

(1) Ten percent of the X-ray counts in the 100–200 keV range come from altitudes above 2500 km, and 45% come from above 2000 km.

(2) The spectral index is the same above and below 2500 km and is taken to be approximately 3.15.

Taken together, these constraints are best satisfied by a model with a broad injection beam (α_0^2 greater than or of order of, say, unity), no coronal trapping, and a column depth down to 2500 km of approximately 1.2×10^{20} cm^{-2}. The electron spectral index, δ, is ~ 3.45.

Because the region above 2500 km has a substantial column depth, the polarizations it gives rise to are not much larger than those seen for the whole flare. The maximum degree of polarization is of the order of 20% for energies up to 100 keV. The degree of polarization for the flare as a whole is less than 10% for all energies greater than 10 keV.

Again, had HXIS imaged this "typical" flare, it would have seen a loop which was approximately 2.8 times brighter at the top than at the footpoints in the energy range 11.5–30 keV.

V. CONCLUSIONS

The two examples of the previous section serve to illustrate several points when one constructs models based on X-ray observations:

1. Observations of limb flares have the distinct advantage that they are not complicated by the contribution of the photospheric albedo.

2. Without any information on the height distribution of the X-rays, we can say little about the flare model parameters. As an absolute minimum we need spectral and flux information from two regions of the flare, as is provided by occultation experiments. If the two regions have the same spectral index, as is the case in the second of our Kane observations, we cannot be as precise as is possible when we have thick and thin target indices. More information on the height distribution of X-rays is crucial for the further development of the models.

3. Polarization measurements in conjunction with height distribution data are important. We expect to see polarization at a high enough level from the upper regions of a flare loop that it would be detectable using present-day technology. The detection of large X-ray polarizations would be strong support for the nonthermal model.

4. A moderate degree of convergence of the coronal magnetic field has a large effect on the height distribution of the X-rays. Any considerable rate of convergence for the coronal magnetic field coupled with a typical flare transition-zone column depth would lead to large coronal fluxes of photons of all energies. At low energies the flux from the coronal loop would swamp that from the footpoints. At high energies the coronal flux would be considerably in excess of what we may be led to expect going by presently available results. Thus we may tentatively conclude that the strength of the magnetic field defining the coronal loop must be approximately constant. This is similar to the indicated results from analyses of high spatial resolution and microwave observations of flares (Petrosian 1982).

This work was supported by the National Aeronautics and Space Administration under grant NSG 7092 and by the National Science Foundation under grant ATM 81-16989.

REFERENCES

Bai, T., and Ramaty, R. 1978, *Ap. J.*, **219**, 705.
Brown, J. C. 1971, *Solar Phys.*, **18**, 489.
_____. 1972*a*, *Solar Phys.*, **25**, 158.
_____. 1972*b*, *Solar Phys.*, **26**, 441.
_____. 1973, *Solar Phys.*, **31**, 143.
_____. 1975, in *IAU Symposium 68, Solar, Gamma-, X-, and EUV Radiation*, ed. S. R. Kane (Dordrecht: Reidel).
Brown, J. C., and Hayward, J. 1981, *Solar Phys.*, **73**, 121.
Brown, J. C., Hayward, J., and Spicer, D. S. 1981, *Ap. J.* (*Letters*), **245**, L91 (BHS).
Brown, J. C., and McClymont, A. N. 1975, *Solar Phys.*, **41**, 135.
Brown, J. C., Melrose, D. B., and Spicer, D. S. 1979, *Ap. J.*, **228**, 592.
Chandrasekhar, S. 1960, *Radiative Transfer* (New York: Dover), p.24.
Craig, I. J. D., and Brown, J. C. 1976, *Astr. Ap.*, **49**, 239.
Crannell, C. J., *et al.* 1978, *Ap. J.*, **223**, 620.
Elwert, G. 1939, *Ann. Phys.*, **34**, 178.
Emslie, A. G. 1980, *Ap. J.*, **235**, 1055.
_____. 1981, *Ap. J.*, **244**, 653.
Gluckstern, R. L., and Hull, M. H. 1953, *Phys. Rev.*, **90**, 1030.
Gluckstern, R. L., Hull, M. H., and Breit, G. 1953, *Phys. Rev.*, **90**, 1026.
Haug, E. 1972, *Solar Phys.*, **25**, 425.
Henoux, J. C. 1975, *Solar Phys.*, **42**, 219.
Hoyng, P., *et al.* 1981*a*, *Ap. J.* (*Letters*), **244**, L153.
Hoyng, P., *et al.* 1981*b*, *Ap. J.* (*Letters*), **246**, L155.
Hudson, H. S. 1972, *Solar Phys.*, **24**, 414.
Kane, S. R. 1974, in *IAU Symposium 57, Coronal Disturbances*, ed. G. Newkirk (Dordrecht: Reidel).
_____. 1980, *Ap. Space Sci.*, **75**, 163.
Kane, S. R., Anderson, K. A., Evans, W. D., Klebesadel, R. W., and Laros, J. G. 1979, *Ap. J.* (*Letters*), **233**, L151.
Kane, S. R. *et al.* 1980, in *Proc. 2d Skylab Workshop, Solar Flares* (Team 4 Rept.), ed. P. A. Sturrock (Boulder: University of Colorado Press).
Kane, S. R., Fenimore, E. E., Klebesadel, R. W., and Laros, J. G. 1982, *Ap. J.* (*Letters*), **254**, L53.
Knight, J. W., and Sturrock, P. A. 1977, *Ap. J.*, **218**, 306.
Langer, S. H., and Petrosian, V. 1977, *Ap. J.*, **215**, 666.
Leach, J., and Petrosian, V. 1981, *Ap. J.*, **251**, 781 (Paper I).
Petrosian, V. 1973, *Ap. J.*, **186**, 291.
_____. 1982, *Ap. J.* (*Letters*), **255**, L85.
Santangelo, N., Horstman, H., and Horstman-Moretti, E. 1973, *Solar Phys.*, **29**, 143.
Smith, D. F., and Brown, J. C. 1980, *Ap. J.*, **242**, 799.
Smith, D. F., and Lilliequist, C. G. 1979, *Ap. J.*, **232**, 582.
Tindo, I. P., Shuryghin, A. I., and Steffen, W. 1976, *Solar Phys.*, **46**, 219.
Van Beek, H. F., *et al.* 1980, *Solar Phys.*, **65**, 39.
Van Beek, H. F., *et al.* 1981, *Ap. J.* (*Letters*), **244**, L157.

Note added in proof.—Owing to a recalibration of instruments (Kane, private communication), the data for the flare of 1978 October 5 have changed. The data as they now stand are: $\gamma_{ISEE3} \approx 3.4$ over the 10–100 keV range, $\gamma_{PVO} \approx 2.3$ over the 100–1000 keV range, PVO/ISEE3 flux ratio above 100 keV ≈ 300.

The model which best fits the new data has an electron spectral index $\delta = 2.6$, an injected beam with $\alpha_0^2 = \infty$, and no magnetic trapping. The column depth from the top of the loop down to an altitude of $h = 25{,}000$ km is now approximately 1.2×10^{19} cm^{-2}. This will give a mean density of 4×10^9 cm^{-3} in the corona.

The data now require a broad injected beam (large α_0^2), and we can no longer expect to see high polarizations. We obtain polarizations of approximately 10% at the top of the loop and 4% for the whole loop as seen by PVO. Similarly, to HXIS this flare would now appear only 4 times brighter at the footpoints than at the top of the loop in the energy range 10–22 keV.

In this case stereoscopic polarization measurements would not have provided further constraints on the modeling. However, polarization results may still be important if obtained in conjunction with height distribution data. We may expect to see high degrees of polarization from the top of a partially occulted flare loop, provided the visible region has a small total column depth (i.e., is a thin target at the X-ray energies being observed) and the electron beam is to some degree collimated. The detection of significant X-ray polarization would still be strong support for nonthermal models, though the absence of high polarization does not necessarily invalidate the nonthermal model.

JOHN LEACH: Institute for Plasma Research, Stanford University, Stanford, CA 94305

VAHÉ PETROSIAN: Institute for Plasma Research, Stanford University, Stanford, CA 94305